CHAPTER

6

The role of secondary craters on Martian crater chronology

Tyler M. Powell[a,*], *Lior Rubanenko*[a,b], *Jean-Pierre Williams*[a] *and David A. Paige*[a]

[a]Department of Earth, Planetary, and Space Sciences, University of California, Los Angeles, CA, United States; [b]Department of Geological Sciences, Stanford University, Stanford, CA, United States

*Corresponding author

Abstract

The influence of secondary craters on the accuracy of crater chronology has been heavily debated. We review the production of secondaries on Mars and their cumulative effect on the global crater size-frequency distribution (SFD). We characterize the SFD of secondaries produced by four large primaries (~50–220 km) and develop a model for secondary accumulation with time, accounting for spatial clustering. The number of km-scale secondaries produced globally may exceed primaries by an order of magnitude on Ga timescales. However, most secondaries are clustered around their parent primary, and regions far from large primaries have lower concentrations of secondaries. We estimate that the crossover diameter between primaries and secondaries on a median surface exceeds 1 km after ~1–2 Ga, though subsequent crater erasure has significantly influenced the number of secondaries visible today. Because of the high spatial variability of secondaries, care should be taken when using small craters for crater counts.

1 Introduction

Impact craters dominate the landscapes of many planetary bodies. On Mars, a variety of geologic processes active throughout its past have erased pre-existing craters, resulting in some regions with very few craters, and other regions that have retained a high spatial density of craters from billions of years of bombardment. Early studies recognized that the relative abundance of impact craters on a surface could be used as an indicator of its age (Baldwin, 1949; Kreiter, 1960; Öpik, 1960; Shoemaker et al., 1963). Lunar samples obtained from the Apollo missions provided radiometric and cosmic ray exposure ages for several regions of the Moon, and crater counts in these regions were used to calibrate models of the absolute cratering rate (Arvidson et al., 1975; Neukum, 1983; Hartmann and Neukum, 2001; Neukum et al., 2001; Stöffler and Ryder, 2001; Robbins, 2014). The field of "crater chronology" has since become one of the most fundamental tools in planetary science and is the principal method of estimating surface

http://dx.doi.org/10.1016/B978-0-12-820245-6.00006-9

age throughout the solar system. An understanding of crater chronology is critical to interpreting the timing of major events in Mars' past.

Primary impact craters form when asteroidal or cometary material collides with the surface at hypervelocity, ~10 km/s on average for Mars (Ivanov, 2001). This results in the formation of a roughly circular depression (Melosh, 1989). Some of the ejected target material fragments are energetic enough to form craters of their own upon re-impacting the surface; these are termed secondary craters or "secondaries." Primary craters are often surrounded by a swarm of smaller secondary craters; single primary impacts have been shown to produce 10^6–10^9 secondary craters, which form nearly instantaneously in geologic time (Bierhaus et al., 2001; McEwen et al., 2005; Dundas and McEwen, 2007; Preblich et al., 2007; Williams 2018). This introduces a complication for crater chronology, which relies on the predictable accumulation of craters with time following a knowable size distribution and rate. The effect of secondary craters on the ages derived from crater counting has been heavily debated since the 1960s. In the last few decades, several high-resolution and high-quality imaging datasets with good global coverage have become available for Mars which allow us to better constrain the production of primary and secondary craters and assess the importance of secondaries for crater chronology there. In this work, we (1) review the history of the secondary crater literature, (2) use a global catalog of Martian craters to constrain the number of secondaries produced by several large primary craters (~50–220 km), and (3) present a new model for the global accumulation of secondary craters with time, including the effect of spatial clustering of secondaries around large primaries.

2 Review of crater size-frequency distributions

The size-frequency distribution (SFD) of craters can be approximated as a power law, often expressed using the cumulative SFD (Crater Analysis Techniques Working Group, 1979):

$$N = CD^{-b} \tag{6.1}$$

where N is the number of craters larger than diameter D, C is a coefficient, and b is a power-law index that controls the ratio of large craters to small craters. This appears as a straight line on a plot of log D versus log N with a slope of $-b$. The cumulative representation is commonly used due to its simplicity; a list of crater diameters can be sorted in descending order and plotted against their rank, where the largest diameter occurs at $N = 1$. The cumulative number of craters is often divided by the count area, A, to produce a spatial density. In this chapter, we will denote absolute crater number using capital letters and crater spatial density using lowercase letters: $n = cD^{-b}$ where $c = C/A$.

The differential SFD is the derivative of the cumulative SFD, or the number of craters within some diameter range divided by the bin width (Crater Analysis Techniques Working Group, 1979):

$$\frac{dN}{dD} = bCD^{-(b+1)} \tag{6.2}$$

While less intuitive than the cumulative SFD, the differential SFD corresponds to the number of craters within some size range and is not affected by the distribution of all larger craters.

In practice, crater populations do not strictly follow a single power law across all diameters. However, this approximation is often appropriate for describing craters within limited size ranges, and the concept of power-law slope is valuable for discussing variations in more complicated crater SFDs. Production functions (PFs) describe the SFD of craters produced on a planetary surface during some time. The commonly used Neukum PF (Neukum et al., 2001) and Hartmann PF (Hartmann, 2005; Hartmann and Daubar, 2017) were developed using the observed SFD of lunar craters. The historical cratering rate was determined by correlating the absolute ages of lunar samples to crater counts on related geologic

units (Arvidson et al., 1975; Neukum, 1983; Hartmann and Neukum, 2001; Neukum et al., 2001; Stöffler and Ryder, 2001; Robbins, 2014). This rate has been relatively constant during the last 3 Ga, with a much higher flux prior to this. In the absence of datable surface samples for Mars, the Martian Neukum/Ivanov and Hartman PFs have been scaled from their lunar counterparts by accounting for differences in the mean impact velocity, gravity, and proximity to the asteroid belt between the two bodies (Ivanov, 2001; Hartmann, 2005; Hartmann and Daubar, 2017). The Martian Hartmann PF also includes a correction for the loss of small craters due to atmospheric effects (Hartmann, 2005). PFs can also be developed using the SFD of the impactor population instead of crater counts. For example, the Williams PF uses the observed flux of bolides entering the Earth's atmosphere (Brown et al., 2002) and crater scaling relationships (Holsapple, 1993) to model the primary PF for the Moon and Mars (Williams et al., 2014). Rubanenko et al. (2021) (Chapter 5: Challenges in Crater Chronology on Mars as Reflected in Jezero Crater) discuss crater SFDs and the application of crater chronology in more detail.

3 Review of the debate over the effect of secondary craters

The first studies to discuss the size distribution of impact craters were performed using the smallest craters on the Moon observable through Earth-based telescopes (Young, 1940). Hartmann (1964) measured the distribution of lunar craters larger than ~8 km in diameter and reported a slope of approximately −2 (note unless otherwise specified, slopes given in this chapter are cumulative). In 1964 the Ranger VII mission to the Moon imaged Mare Cognitum at high resolution, providing the first observations of features smaller than ~100 m on the lunar surface. This expanded the lunar crater SFD to significantly smaller sizes. Shoemaker (1965) found that the SFD of craters smaller than ~1 km has a slope of approximately −3.5, significantly steeper than the slope observed for larger craters. This is sometimes referred to as the "steep branch" of the SFD, relative to the "shallow branch" for craters larger than ~1 km. Clusters of secondary craters associated with the ray systems of nearby large primary craters were abundant in Mare Cognitum images. Shoemaker (1965) classified craters as primary or secondary based on their clustering and morphology. Secondaries found close to large primaries tend to be shallower in depth than primaries of the same size and have irregular shapes (Shoemaker, 1965). They often form in distinct clusters or chains, sometimes so closely packed that they create elongate composite craters (Fig. 6.1A and B). This distinctive morphology is likely caused in part by the relatively low velocities and close proximity of impactors (Shoemaker, 1965; Melosh, 1989). Farther away from the primary, secondaries become less clustered and greater impact velocities result in more circular secondary craters (Fig. 6.1C and D). These distant secondaries, sometimes termed "field," "background," or "unrecognized" secondaries, can be more difficult to distinguish from primary craters.

Shoemaker (1965) states that the fraction of secondaries in Mare Cognitum becomes larger at smaller sizes: most craters larger than 1 km were classified as primary while the majority of craters between 300 m and 1 km were classified as secondary. Counts of secondaries around large lunar primaries (Shoemaker, 1965; Wilhelms et al., 1978) and terrestrial explosion craters (Roberts, 1964) revealed power-law slopes of roughly −4, similar to the steep slope observed for lunar craters smaller than ~1 km. Shoemaker (1965) proposed a model of total crater accumulation where primary craters dominate at large sizes but secondary craters overtake them below some "crossover diameter," which varies by terrain age (discussed further later) and Shoemaker (1965) estimates is ~200 m for the lunar maria. Shoemaker's argument has sometimes been interpreted to be that the "steep branch" observed in the SFD below

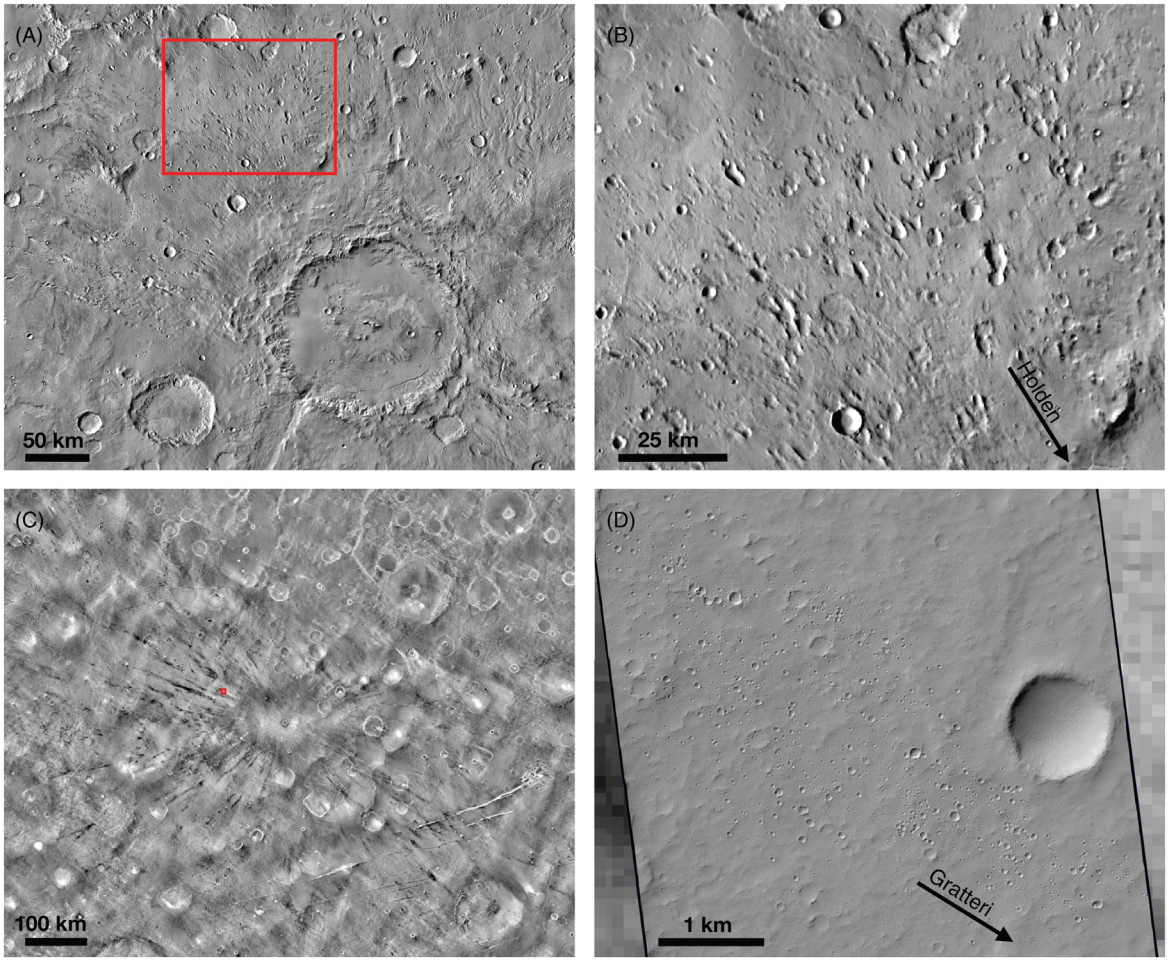

FIGURE 6.1 Two examples of primary craters with systems of secondary craters. (A) Holden crater (153.8 km, −26.4°N, −34.0°E) and (B) a field of nearby secondaries in the THEMIS daytime IR Global Mosaic (Edwards et al., 2011). (C) Gratteri crater (6.9 km, −17.7°S, −160.1°E) showing distinctive low thermal inertia rays extending several hundred kilometers in the THEMIS nighttime IR Global Mosaic (Edwards et al., 2011). (D) A High Resolution Imaging Science Experiment (HiRISE) image of a cluster of secondaries ~120 km or ~34 crater radii from Gratteri crater (HiRISE EPS_026579_1630). Secondaries close to their primary tend to have distinctive irregular morphologies, while distant secondaries are more circular and can be difficult to distinguish from primaries.

1 km is caused predominantly by secondary craters. However, Shoemaker preferred a model for primary production that included a steepening at smaller sizes based on the size distribution of near-Earth objects (Brown, 1960), which is consistent with our current understanding of sub-km primary production in the inner solar system (Ivanov, 2006; Williams et al., 2014; Speyerer et al., 2016). Soderblom et al. (1974) adapted this model for Mars and proposed that most of the craters smaller than 1 km on Mars were of secondary origin.

While secondaries clearly contribute to observed crater populations, there has been disagreement on the effect that secondaries have on the validity of crater chronology. The Hartmann

PF excludes obvious secondary craters but includes both primaries and some unknown fraction of background secondaries, making the assumption that the more randomly distributed background secondaries also record chronological information (Hartmann and Daubar, 2017). Some have argued that the majority of secondaries can be identified by their morphology or clustering, and therefore secondaries have a minimal influence on derived surface ages if obvious secondaries are carefully excluded from crater counts (König, 1977; Neukum et al., 1975, 2001). Because the largest craters on the surface contribute most of the secondary craters, the crossover diameter should progress to larger sizes for older terrains (Neukum, 1983, Neukum and Ivanov, 1994; Werner et al., 2009). This effect is illustrated well by the results of Wilhelms et al. (1978) who found that secondaries formed by lunar basins result in a crossover diameter in the highlands of ~20 km, much larger than the 200 m value Shoemaker (1965) proposed for the younger Maria. Neukum and Ivanov (1994) found that when "obvious" secondaries were excluded from counts, the SFD maintained an increase in slope for craters smaller than ~1 km for terrains of all ages and argued that this meant that the PF reflected predominantly primaries. The observation of a steep slope for 200–600 m diameter craters on Gaspra, which is expected to have very few secondaries because of its low escape velocity, provided additional evidence that the primary impactor population includes a steepening below ~1 km (Chapman et al., 1996).

Others have noted that secondary craters sufficiently far from their parent primary look nearly indistinguishable from primary craters of the same size and are often not clearly clustered (Shoemaker, 1965; Soderblom et al., 1974; McEwen and Bierhaus, 2006). This is exemplified by young Martian craters with well-preserved secondary-containing ray systems, which extend hundreds of crater radii in some cases (McEwen et al., 2005; Tornabene et al., 2006; Preblich et al., 2007; Quantin et al., 2016; Williams, 2018; Williams et al., 2018), as revealed by their thermal signature observed by the Thermal Emission Imaging System (THEMIS) on the Mars Odyssey spacecraft (Christensen et al., 2004). In particular, a ~10 km rayed crater on Mars, Zunil (7.7°N, 166.2°E), is estimated to have produced $\sim 10^8$ secondary craters larger than 10 m in diameter (McEwen et al., 2005; Preblich et al., 2007). This is comparable to the number of primary craters of the same size expected to have been produced during the last few Ma, the estimated age of Zunil. Almost all of these were formed at ranges greater than ~16 crater radii and lack the distinctive morphological characteristics commonly used to identify secondary craters. This finding, as well as a similar study of secondary craters on Europa published around the same time (Bierhaus et al., 2005), led to renewed interest in the problems that secondaries could pose for chronology models. This led some researchers to suggest that the small crater population on Mars may be dominated by "field" or "background" secondaries of distant large primaries and that the PFs developed from crater counts excluding only obvious secondaries may not be representative of the primary crater population (McEwen and Bierhaus, 2006). Modeling work by Bierhaus et al. (2018) demonstrates that there is likely significant variation in the expression of secondary crater populations throughout the solar system, depending on effects like surface gravity, escape velocity, and typical impact velocity. For example, field secondaries may be especially important for the Moons of Saturn, where their relatively low surface gravities result in more globally distributed secondaries. Conversely, bodies with high surface gravity like the Moon and Mars show more clustered secondary fields. This results in a high regional variability in crater spatial density.

These stances have not yet been fully reconciled. Ultimately, the relative importance of secondaries can be determined if both (1) the production rate of primaries and (2) the distribution

of secondaries produced by individual primaries are known. While conceptually simple, obtaining definitive measurements for either of these has proved complicated, though modern datasets with high resolution and global coverage are providing valuable insights. We address both components in the following sections.

4 Constraining the flux of small primary craters

One of the largest debates in the study of secondary cratering is: Do commonly used PFs largely reflect primary crater production, or have they been significantly influenced by secondary craters and thus represent the accumulation of primaries plus some unknown fraction of secondaries? The identification of several small craters formed on Mars within the last few decades provides a unique opportunity to isolate the current primary cratering rate. Malin et al. (2006) identified 19 new craters using the Mars Orbiter Camera (Malin et al., 1992) on the Mars Global Surveyor spacecraft. New craters were identified by the appearance of dark spots in repeated imagery, which result from the removal of a surface layer of bright dust by the impact blast. Daubar et al. (2013, 2014) expanded this survey using observations from the Context Camera (CTX) (Malin et al., 2007) and High Resolution Imaging Science Experiment (HiRISE) (McEwen et al., 2007). The most recently published SFD includes 110 impacts with dates constrained by CTX before and after images (Daubar et al., 2014). Over half of the impact sites are clusters of craters instead of individual primary craters due to fragmentation of the impactor in the atmosphere. Effective crater diameters for the clusters were estimated by summing the volumes of craters within each cluster: $D_{eff} = \left(\sum_i D_i^3\right)^{1/3}$ (Malin et al., 2006; Daubar et al., 2013; Ivanov et al., 2014). The effective diameters of these impacts range from ~1 to ~40 m. These are expected to be primaries as they appear across extensive areas of Mars and have a range of formation dates. Additionally, creating secondaries of this size would require a primary crater at least a few 100 m in diameter (Schultz and Singer, 1980), which has not been observed.

Fig. 6.2 shows the SFD of new Martian craters identified by Daubar et al. (2013, 2014). The number of new craters ~15 m in diameter is three to five times lower than predicted by the Hartmann and Ivanov PFs. The SFD of new craters also has a shallower slope than either PF in this size range, resulting in better agreement with

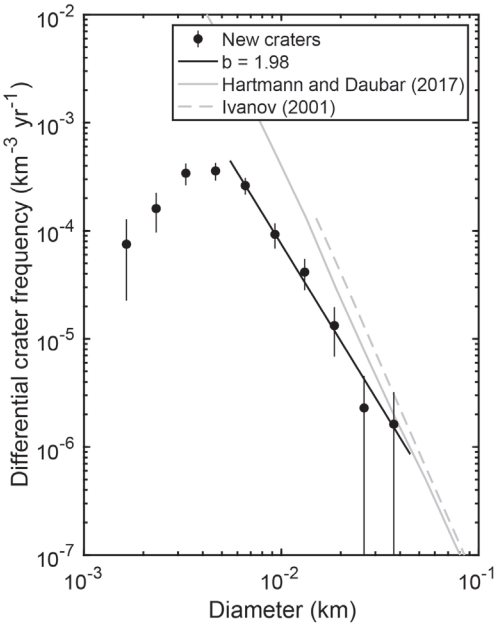

FIGURE 6.2 New primary craters observed by the High Resolution Imaging Science Experiment (Daubar et al., 2013, 2014) in root-2 bins normalized to an annual flux. Note that in the figure in Williams (2018), data were plotted at bin edges rather than the geometric bin centers as is done here. The SFD of ~15 m new craters identified on Mars is approximately three to five times lower than expected from the production functions. The best fit differential slope is −2.98 (or $b = 1.98$) for craters larger than 5.5 m. *Modified from Williams (2018).*

the PFs for the largest new craters observed. The cause for these discrepancies is currently unresolved, though several possible explanations have been proposed.

One option is that the counts used to derive the PFs include unrecognized field secondaries, resulting in an overprediction of the number of decameter-sized craters. Hartmann et al. (2018) use the observation that ~50% of new craters form clusters to estimate the secondary contribution for several regions of Mars. They propose that the total number of primary craters in a region should be roughly double the number of clusters, and that any additional individual craters may be field secondaries. Using this approach, they estimate that ~40–80% of craters ~20–250 m in diameter may be field secondaries, with greater percentages at smaller sizes. The catalog of new craters likely oversamples crater clusters because their larger footprint is easier to detect from orbit than the equivalently sized individual primary (Daubar et al., 2019), so these results may be an upper bound. Williams et al. (2014) demonstrate that a PF developed using the current flux of terrestrial bolides agrees with the Hartmann PF. Because the Williams PF represents only primary impacts, this result indicates that the Hartmann PF should contain relatively few secondaries in the decameter size range. Additionally, the formation rate of new craters on the Moon agrees with the lunar Neukum PF, differing by only ~33% (Speyerer et al., 2016). This suggests that secondary craters do not make a significant contribution to the lunar PFs, from which their Martian counterparts are derived.

The catalog of new Martian impacts is also known to be incomplete. Because new impacts are detected by the formation of dark spots, the catalog is biased toward the dustiest areas of Mars. This was addressed in Daubar et al. (2013) by considering only regions with a high dust cover index. However, Daubar et al. (2014) show that dark spots are not uniformly distributed even in dusty regions. Compensating for spatial variations in detection efficiency may increase the new crater SFD by a factor of ~1.7 or more. This may also partially explain the shallow slope of the new crater SFD, as it is likely that small craters are more affected by the variations in the terrain properties that cause non-uniform dark spot detection (Daubar et al., 2015). Additionally, dark spots may fade due to Aeolian processes. A study of dark spot changes over time shows that the median blast zone has a lifetime of ~8 Martian years, an order of magnitude longer than the average interval between CTX images for detected dark spots (Daubar et al., 2016). However, some small craters do show more rapid changes and some potentially may fade prior to detection.

Alternatively, ablation or deceleration of impactors in the atmosphere could result in smaller craters, especially if fragmentation occurs prior to impact. The Hartmann PF and Williams PF account for the influence of the atmosphere on crater size (Popova et al., 2003), though it is possible that these models underpredict this effect (Ivanov et al., 2014). It is also possible the observed SFD is the result of real fluctuations in the impact rate. While current crater chronologies suggest that the cratering rate has been relatively constant over the last ~3 Ga, it may vary on short timescales due to collisions or breakup events in the asteroid belt, but it is still under investigation at what crater diameters this effect would be noticeable (Bottke et al., 2007; Nesvorný et al., 2009; Vokrouhlický et al., 2017; Mazrouei et al., 2019; Terada et al., 2020; Kirchoff et al., 2021).

Considering the many assumptions involved with developing a crater chronology for Mars and the complicated processes that may influence new crater detection, the agreement of the new crater SFD with the Hartmann and Ivanov PFs is generally quite good. The observed discrepancy likely results from some combination of the previously discussed effects. However, regardless of the dominant cause, these results confirm that the "steep branch" of the Martian SFD observed for craters <1 km cannot solely be attributed to secondaries. An extrapolation

of the "shallow branch" to these smaller sizes underpredicts the number of new craters by a factor of $\sim 10^2$, much greater than the observed discrepancy of 3–5.

5 Production of secondaries by Martian primaries

The total number and size distribution of secondaries produced by individual primaries has proven difficult to fully characterize observationally. The common approach is to consider only obvious secondaries using indicators like clustering or by their distinctive morphology, including location in rays. Shoemaker (1965) identified obvious secondary craters around Langrenus crater (130 km, −8.9°N, 60.9°E) on the Moon and found that the SFD approximately followed a power-law distribution with a slope of roughly −4. The largest secondary identified around Langrenus was ∼5% the size of the primary. This agreed fairly well with counts of secondaries around the Sedan nuclear explosion crater (390 m) on Earth which also showed a slope of −4, though the largest secondary was ∼8% the size of the primary (Shoemaker, 1965). Schultz and Singer (1980) studied the secondary populations of a small sample of large craters on the Moon, Mercury, and Mars and found that few secondaries are formed larger than 5% the size of the primary, though examples of larger secondaries are not uncommon. Target properties also influence secondary production on Mars. Calahorra crater (34.2 km, 26.45°N, −38.65°E), which formed in Chryse Planitia, showed a similar ejecta structure and secondary distribution to craters on Mercury and the Moon (Schultz and Singer, 1980). However, Arandas crater (24.8 km, 42.41°N, −15.03°E) and Davies crater (48.1 km, 45.96°N, 0.09°E), which formed in the fractured plains region and have extensive flow lobes, showed very few secondaries larger than 2% of their diameter.

Robbins and Hynek (2011b) use a global database of all Martian craters larger than 1 km (Robbins and Hynek, 2012) to examine the secondary populations of 24 large Martian primaries ∼20 to ∼220 km in diameter. They classify craters in their nearby secondary field as primaries or secondaries using morphological indicators. The secondary SFDs have a wide range of power-law slopes between −3.3 and −8 over certain diameter ranges. The secondaries considered in this survey typically peak in number at 2.4 crater radii and extend to roughly 6 crater radii. Robbins and Hynek (2011a) studied the distant secondaries of Lyot crater (220 km, 50.8°N, 29.3°E) and identified ∼150 clusters of secondaries as far as 5200 km or ∼50 crater radii away. The number of distant craters identified is about an order of magnitude fewer than the number of secondaries proximal to Lyot crater, though this is an underestimate as only clusters of secondaries were included. However, this demonstrates that secondary contamination can occur even in regions that are far from large primaries. Robbins and Hynek (2014) catalog all Martian craters as primary or secondary and estimate that at least 19% of the craters >1 km globally are secondaries. This study presents a conservative underestimate, as many distant secondaries which lack clear morphological indicators were likely not identified.

Several other rayed craters in addition to Zunil were identified in THEMIS nighttime imagery (Tornabene et al., 2006). Quantin et al. (2016) performed crater counts on and between the rays of Gratteri crater (6.9 km, −17.7°N, −160.1°E). They estimate that half of the secondaries of Gratteri crater are located within rays and clusters that occupy 2% of the area around Gratteri, and the other half are scattered between obvious rays. Corinto crater (13.8 km, 16.95°N, 141.72°E) is a rayed crater in Elysium Planitia. Williams et al. (2018) and Williams (2018) performed counts of meter-to-decameter-sized craters in two regions overlapped by Corinto rays at distances of 520 and 660 km. The crater SFDs deviate from the Hartmann PF at small sizes in both locations, with steep power law slopes varying from −3.6 to −8.2 over limited size ranges. Regions not overlapped by obvious rays also show this increase in slope, though the total spatial density

of craters in inter-ray regions is lower than inside rays. Williams (2018) estimates that Corinto crater may have produced over 10^9 meter-to-decameter-sized secondary craters.

Zunil and Gratteri craters have few secondaries within 10 crater radii with their largest secondaries ~2% the size of the primaries. This contrasts notably with the densely packed fields of proportionately larger secondaries observed around 100 km-scale primaries (Schultz and Singer, 1980; Robbins and Hynek, 2011b). Preblich et al. (2007) note that few large blocks are found around Zunil and suggest that small fragments, which landed within a few crater radii, and consequently had lower velocities, may not have been energetic enough to form noticeable secondary craters. However, the reason for this difference remains an open question.

Vickery (1986, 1987) studied the secondary fields of several primaries on the Moon, Mercury, and Mars and found that the maximum secondary size decreases with distance from the primary. This was used to characterize the size–velocity relationship of ejecta fragments. The ejection velocity for each secondary was determined from their range to the primary. Crater scaling laws (Schmidt and Holsapple, 1982; Schmidt and Housen, 1987) were used to infer the size of the inciting ejecta fragment from the secondary crater size. The upper envelope of ejecta fragment size and ejection velocity was fit using a power law: $d_{max} \propto v^{-\beta}$ where the velocity exponent β typically varied between ~1.5 and 2.5 (Vickery, 1987). Singer et al. (2020), in a study of the secondary fields of several lunar craters, show that variation in β likely depends on the size of the primary crater. The maximum ejecta fragment size falls off more rapidly with velocity for larger primary craters.

5.1 New measurements of secondaries around large Martian primaries

Robbins and Hynek (2011b) noted that the regions surrounding several large primaries show an enhancement in the total spatial density of craters a few kilometers in diameter and steep-sloped SFDs. This indicates that the effect of secondaries is noticeable in these regions even without classifying craters as primary or secondary. A less explored method for estimating secondary production is to compare the SFD of all craters between a region proximal to a large primary and a nearby reference region of similar age and geology. Subtracting the SFDs between these two regions results in a distribution of "excess" craters which we assume to be mostly secondaries. A major advantage of this approach is that it is agnostic to classification criteria like morphology or clustering. We use this approach and a catalog of Martian craters >1 km (Robbins and Hynek, 2012) to investigate four large primary craters, three of which were also studied in Robbins and Hynek (2011b). For each, we consider a region extending to ~8 crater radii, beyond which the crater spatial density is indistinguishable from the background spatial density (Robbins and Hynek, 2011b). Reference regions were selected which occur on similar terrain and are likely to be of similar age. Lomonosov crater (120 km, 64.9°N, −9.2°E) is located in the relatively sparsely cratered Northern Plains, which causes the excess crater spatial density in its vicinity to be easily noticeable (Fig. 6.3A). Lyot crater (220 km, 50.5°N, 29.3°E) is also located in the Northern Plains; however, many of the secondaries to the south overlap a more heavily cratered landscape (Fig. 6.3B). To avoid this complication, we only consider the region north of Lyot crater and assume that the same number of secondaries was produced in the south. We also investigate an unnamed 77.6 km crater (−30.28°N, −160.18°E) and 50.8 km Kalpin crater (8.93°N, 141.28°E).

One limitation of this approach is that it is often difficult to identify large, uninterrupted regions with similar age and geology on Mars. As a result, many primary craters with prominent secondary fields are poor candidates for this method because their secondaries overlap

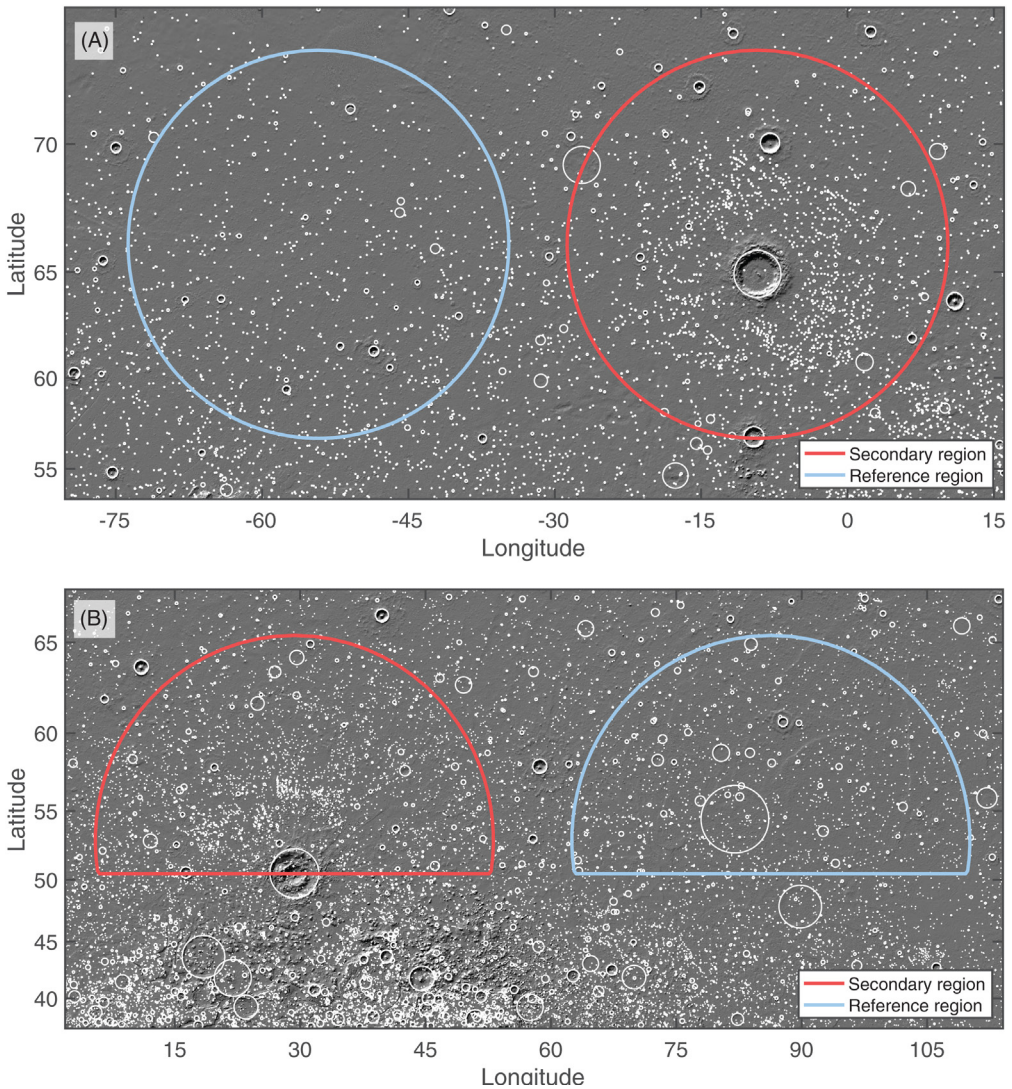

FIGURE 6.3 Craters larger than 1 km in regions around (A) Lomonosov crater (120 km) and (B) Lyot crater (220 km) from the Robbins and Hynek (2012) crater catalog. Data are overlaid on the Mars Orbiter Laser Altimeter (MOLA) shaded relief map (Smith et al., 2001). The Mercator projection is used to preserve crater shape in the high latitudes. The count region around each crater extends to 8 crater radii. For Lyot crater, we only consider the northern half of this 8 crater radii annulus as a change in terrain type to the south causes an increase in crater spatial density not related to secondaries. Both primaries show a noticeable excess of small craters (1–10 km) in this region. We compare the SFD in this region to a nearby reference region that likely has experienced a similar number of primary impacts.

more than one terrain type or overlap the secondary fields of other nearby primaries. Additionally, erosional processes that may erase craters, such as infill by regolith or ice deposition/sublimation, can be fairly localized. Crater erasure is further discussed in Rubanenko et al. (2021) (Chapter 5: Challenges in Crater Chronology on Mars as Reflected in Jezero Crater).

We minimize these effects by focusing on craters found in expansive regions of similar terrain and with relatively uniform background crater densities like the Northern Plains, as these regions are likely to have experienced a similar history of primary cratering and crater erasure. However, it is important to note that local difference may still persist.

Fig. 6.4 shows the differential crater SFD for each candidate site. The spatial densities of the secondary field regions generally agree with the reference regions for large craters (>10 km), which are expected to be mostly primaries. This indicates that the two regions have similar ages and experienced a comparable primary cratering history. The secondary field regions show

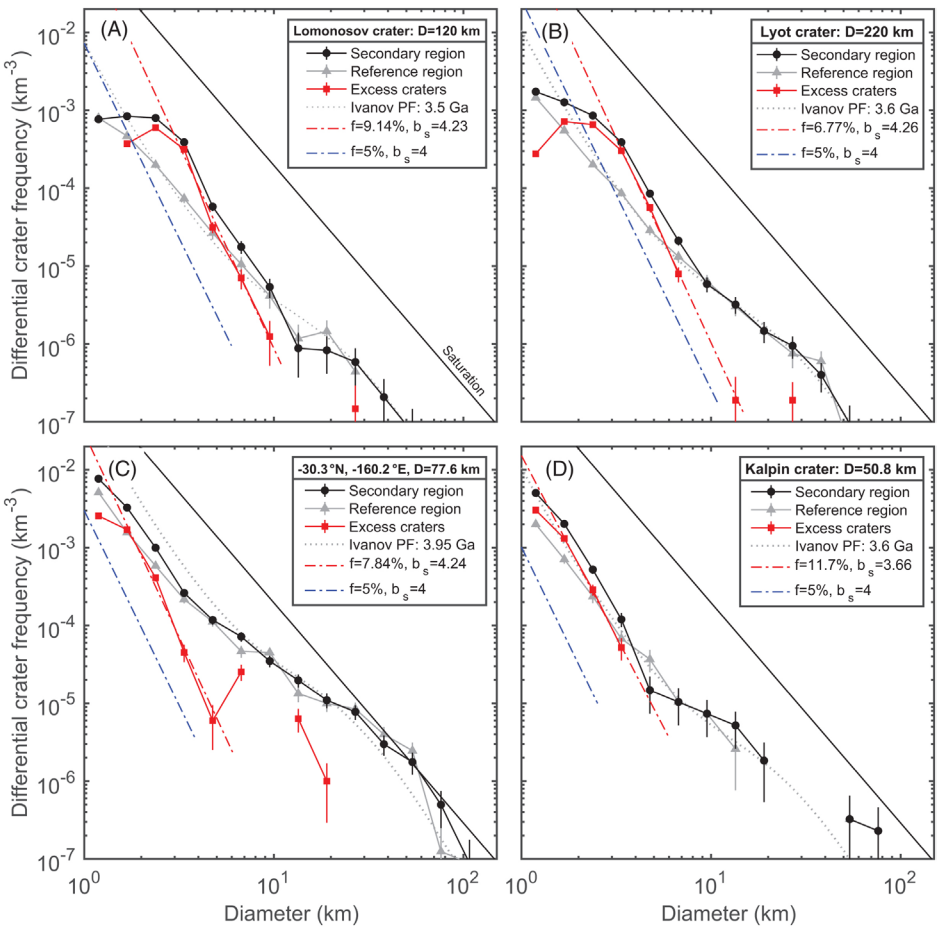

FIGURE 6.4 Differential SFDs of the regions around four Martian craters (A-D) with noticeable secondary fields compared to the SFDs of nearby reference regions. The SFDs generally agree for large diameters (>10 km) but show an excess of small craters (1–10 km) in the secondary field region. For Lyot crater, only the northern secondary field is considered (Fig. 6.3B). We fit the distribution of excess craters to a power law with slope $-b_s$ and a coefficient that is scaled to the size of the primary by f, the ratio of the expected diameter of the largest secondary to the primary diameter (Eq. 6.3). In all cases, more secondary craters are required than would be predicted using values of $f = 5\%$ and $b_s = 4$. The *dotted gray lines* show Ivanov PF isochrons for reference (Ivanov, 2001) and the *solid black lines* indicate saturation equilibrium (Hartmann, 1984).

a noticeable excess of small craters (1–10 km) relative to their reference regions. We assume that this is primarily the result of abundant secondaries. Crater erasure in the reference region may also play a role, though this is unlikely to be the dominant difference due to the choice of regions with similar geologic context. The distribution of excess craters, obtained by subtracting the SFDs between the two regions, is fit using a power law:

$$N_{s,i} = C_{s,i} D^{-b_s} = \left(f D_{p,i}\right)^{b_s} D^{-b_s} \qquad (6.3)$$

where b_s is the power-law slope and $C_{s,i}$ is the coefficient. We express $C_{s,i}$ in terms of the expected size of the largest secondary, which is some fraction, f, the size of the primary, $D_{p,i}$. Note that we do not directly measure the largest secondary. Rather, $fD_{p,i}$ corresponds to what the size of the largest secondary would be if the power law that fits the SFD at smaller sizes continues to $N_{s,i} = 1$.

The slope of the SFDs range from -3.7 to -4.3, consistent with previous studies (Shoemaker, 1965; Wilhelms et al., 1978; Robbins and Hynek, 2011b). However, we require an f of ~7–12% to explain the number of excess craters. This is greater than the 5% value that has been used in studies estimating the global secondary SFD (Soderblom et al., 1974; Werner et al., 2009). While this difference may seem small, $N_{s,i}$ is a strong function of f. Using $f = 5\%$ and $b_s = 4$ underpredicts the number of inferred secondaries by about an order of magnitude (Fig. 6.4). This highlights that using the size of the largest observed secondary to define the secondary SFD at smaller sizes may result in significant errors.

The distribution of inferred secondaries deviates from the power-law fit at small diameters. While the distribution of secondaries is expected to transition to a shallower slope at some diameter (McEwen et al., 2005; Melosh, 1989), we suggest that the roll-off observed in this case is likely due to the erasure of small craters by erosional processes such as crater infill by regolith or ice deposition/sublimation. This is demonstrated by the crater SFDs of the reference regions, which deviate from the PF at small sizes. It is likely that more craters, both primaries and secondaries, were produced in the 1 km size range than are currently represented. Secondaries may be especially susceptible to erasure because they are shallower than primaries of the same size. This roll-off may also be partially due to incompleteness of the Robbins and Hynek (2012) crater catalog in these regions of Mars. The THEMIS daytime IR mosaic (Christensen et al., 2004) that was used to produce the crater catalog had a global coverage of >99% at the time; however, there were some small regions that lacked coverage, particularly in the northern high latitudes (Robbins and Hynek, 2012).

Distant secondaries are also formed at greater ranges than the ~8 crater radii that we consider here. Despite many studies of secondary populations, the total number of distant secondaries has proved difficult to characterize in large part because their spatial density rapidly becomes lower than the spatial density of background primaries. The radial drop-off of inferred secondaries close to the crater, where an excess crater spatial density can be measured, may help to inform the number of distant secondaries. We consider only craters larger than 2.5 km because of the potential erasure of smaller craters. Fig. 6.5 shows the decrease in crater spatial density radially away from Lomonosov and Lyot craters. In both cases, almost no secondaries are formed within 2 crater radii. The secondary spatial density peaks between 2 and 4 crater radii and decreases rapidly beyond this. We characterize this drop-off by fitting a power law to the excess crater spatial density: $n \propto r^{-\alpha}$. For Lomonosov crater, we find an α value of ~4.5 between 3 and 8 crater radii. The spatial density at ~8 crater radii is very close to the spatial density of the reference region, indicating that there are few >2.5 km secondaries at this distance.

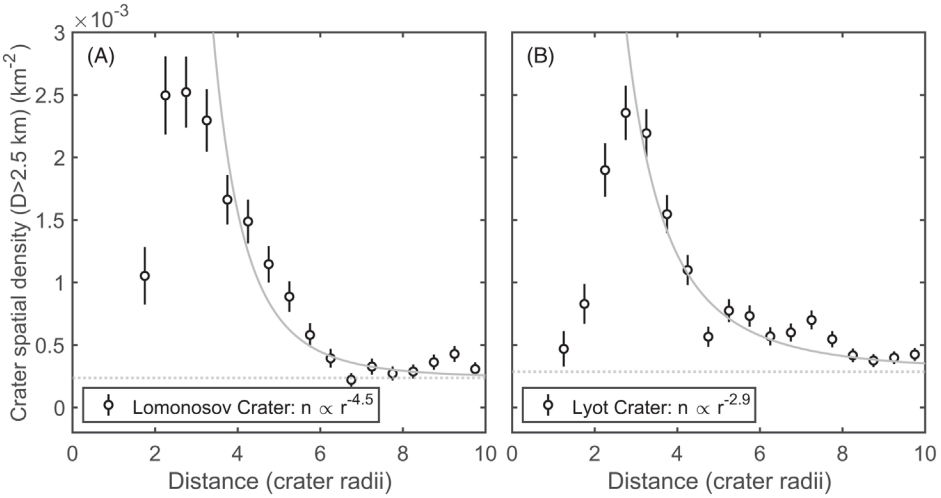

FIGURE 6.5 The decrease in the spatial density of >2.5 km craters radially away from (A) Lomonosov and (B) Lyot crater. A power law is fit to the spatial density above background to characterize the drop-off of inferred secondaries. The background spatial density, indicated by the dotted line, is defined as the spatial density of >2.5 km craters in the reference region.

For Lyot crater, we find an α value of ~2.9, a more gradual drop-off in inferred secondaries than we observe for Lomonosov. There are several possible explanations for this difference: (1) Lyot crater impacted close to the heavily cratered Martian highlands, which may result in more primaries in the region around Lyot than there are in the reference region. Even at a distance of 8–10 crater radii, the crater spatial density is slightly greater than that of the reference region. If the background spatial density in Fig. 6.5B is adjusted to be the average value at 8–10 crater radii, the radial drop-off of inferred secondaries has an α similar to that of Lomonosov. However, the reference and secondary regions agree for large craters (Fig. 6.4B), indicating that both regions are likely sampling fairly similar terrain. (2) Interestingly, the peak crater spatial density around Lyot is slightly lower than around Lomonosov, despite Lyot being significantly larger and presumably capable of producing many more secondaries of any given size. Lyot also requires a lower value of f than Lomonosov (Fig. 6.4B), indicating that Lyot's secondary field contains fewer secondaries than Lomonosov relative to its size. One explanation for this difference may be that many of Lyot's proximal secondaries have been degraded. Inspection of Lyot's nearby secondary field reveals many subdued, irregular depressions that are not classified as craters in the Robbins and Hynek (2012) catalog, but which may have been distinct craters in the past. In comparison, the secondaries around Lomonosov are more circular and have noticeably sharper rims. This could also explain the relatively gradual drop-off of secondaries away from Lyot; if the peak spatial density was greater, this would result in a more rapid drop-off with distance. (3) It is also possible that Lyot simply produced fewer secondaries relative to its size than Lomonosov, and that these secondaries were emplaced at relatively greater distances.

If the drop-off behavior we observe for Lomonosov and Lyot continues beyond the region we consider here, we infer that 70–95% of all secondaries should be between 2.5 and 8 crater radii, and 5–30% may be formed at greater ranges. This is roughly consistent with Robbins and Hynek (2011a) who found about an

order-of-magnitude fewer distant secondaries of Lyot crater than nearby secondaries, though that study did not account for distant secondaries that were not obviously clustered and only clusters with a majority of craters larger than ~1 km were considered. We emphasize that additional work characterizing the number and spatial distribution of distant secondaries is necessary.

6 Model of the global secondary SFD

Soderblom et al. (1974) provide a framework for analytically modeling the global secondary SFD, which we present here with some modifications: (1) we consider a more realistic non–power law PF for primary craters and (2) we consider that the number of secondaries produced by each primary may be greater than previously thought. The global secondary crater SFD is the sum of the secondaries produced by each individual primary (Shoemaker, 1965; Soderblom et al., 1974):

$$N_s = \sum_{i=1}^{\infty} N_{s,i} = \sum_{i=1}^{\infty} \left(f D_p(i) \right)^{b_s} D^{-b_s} \qquad (6.4)$$

where $D_p(i)$ is the diameter of the ith largest primary crater formed on Mars after some time, b_s is the power-law slope of secondaries, and f is the ratio between the size of the expected largest secondary to the size of the primary. This is a slight modification from Soderblom et al. (1974) who integrated over all primaries instead of using a discrete sum. However, our approach is more easily applied to arbitrary primary SFDs. The size distribution of primary craters is determined by a PF. The global secondary SFD can be calculated for any primary PF by solving Eq. (6.4) numerically (our results shown in Figs. 6.6 and 6.7 use the Ivanov PF). However, we first consider the simple case where the primary SFD follows a power-law distribution with a constant cratering rate as this has a closed-form analytical solution. The cumulative

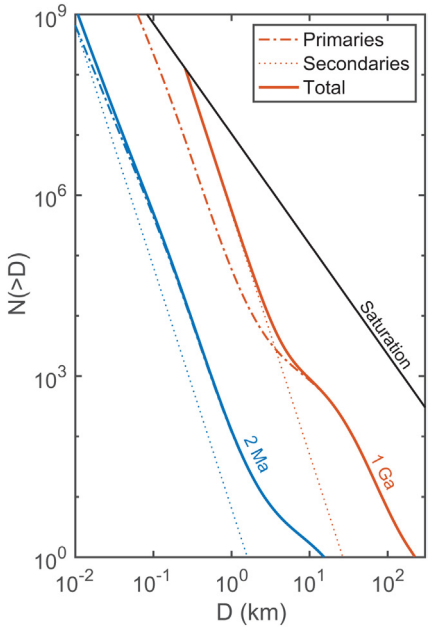

FIGURE 6.6 The predicted global cumulative SFD of primary and secondary craters produced on Mars after 2 Ma and 1 Ga using $f = 10\%$ and $b_s = 4$. The primary SFD is determined by the Ivanov PF. The secondary SFD is determined by summing the SFD of secondaries produced by all primaries (Eq. 6.4). Most km-scale craters are primary on Ma timescales. However, after 1 Ga, secondaries dominate the global SFD for craters smaller than a few kilometers. This demonstrates that the global crossover diameter increases with time. The *black line* indicates saturation equilibrium (Hartmann, 1984).

number of primary craters on Mars after some time assuming a power-law PF is as follows:

$$N_p = CD^{-b_p} = (\gamma A t) D^{-b_p} \qquad (6.5)$$

where A is area (of Mars in this case), t is time, and γ is a constant cratering rate. The primary slope, b_p, has been shown to vary with size but is ~2 on average for craters larger than 1 km. We rearrange Eq. (6.5) to find the diameter of the ith largest crater:

$$D_p(i) = \left(\frac{\gamma A t}{i} \right)^{1/b_p} \qquad (6.6)$$

Substituting Eq. (6.6) into Eq. (6.4), we obtain the cumulative number of secondaries produced by a power-law distribution of primaries:

$$N_s = f^{b_s} \left(\gamma A t\right)^{b_s/b_p} D^{-b_s} \cdot \sum_{i=1}^{\infty} i^{-b_s/b_p} \qquad (6.7)$$

The factor outside of the summation is the expression for the secondary SFD produced by the single largest primary. The summation is a coefficient that scales this to account for all primary craters. For $b_s > b_p$, this converges to the Riemann zeta function, $\zeta\left(b_s/b_p\right)$. For reasonable values of b_s and b_p (~4 and ~2), ζ is ~1.64, so the secondaries produced by the single largest primary account for a large percentage of the total number of secondaries: $1/\zeta \approx 60\%$.

$$N_s = f^{b_s} \left(\gamma A t\right)^{\frac{b_s}{b_p}} \zeta\left(b_s/b_p\right) \cdot D^{-b_s} \qquad (6.8)$$

Eq. (6.8) reveals several interesting behaviors of secondary accumulation not exhibited by primaries. Most notably, secondaries accumulate non-linearly with time, even for a constant primary cratering rate: $N_s \propto t^{b_s/b_p}$. This is because nearly all of the secondaries are produced by the largest several primaries, and the size of the largest primary increases with time (Eq. 6.6). A consequence of this is that the secondary SFD "moves" relative to the primary SFD, causing the crossover diameter to progress to larger sizes for greater ages (Fig. 6.6). This has been noted by several authors (Neukum, 1983; Neukum and Ivanov, 1994; McEwen et al., 2005; Werner et al., 2009; Robbins and Hynek, 2014); however, the expression presented here illustrates why this must be the case. This also shows that background secondaries should not accumulate steadily with time.

The secondary SFD also depends non-linearly on the surface area of the planet as A^{b_s/b_p}; a larger "accumulation surface" will collect larger craters than a smaller one during the same interval. For example, the surface area of Mars is 3.8 times the surface area of the Moon. Ignoring differences in the primary production or secondary formation between these two bodies [though effects like gravity, target properties, and typical impact velocity certainly play a role (Bierhaus et al., 2018)], we might expect a factor of ~14 more secondaries form on Mars than the Moon during the same time interval simply as a consequence of a larger surface area, though preservation differences will significantly influence what is visible today.

The scale factor f^{b_s} indicates that the secondary SFD is extremely sensitive to the distribution of secondaries produced by each primary. Previous studies of global secondary accumulation have used $f \approx 5\,\%$ (Soderblom et al., 1974; Werner et al., 2009). In Section 5.1, we suggest that the population of km-scale secondaries around several large primary craters requires an f that may be as high as 10%. This doubling of f corresponds to an increase in the global secondary SFD by a factor of 16 for $b_s = 4$. Fig. 6.7 shows the evolution of the global mean crossover diameter with time calculated for two PFs: (1) a simple two-branch power-law model with an increase in slope below ~1 km and (2) the Ivanov PF that was calculated numerically from Eq. (6.4). These models agree fairly well when considering ~km-sized craters on Ga timescales, though variations in the Ivanov PF above 1 km result in factor of 2–3 offsets between the two models. Using values of $f = 5\%$ and $b_s = 4$, the global crossover diameter exceeds 1 km after ~1.5–2 Ga, consistent with the findings of Werner et al. (2009). However, for $f = 10\%$, the global crossover diameter exceeds 1 km for surfaces as young as ~20 Ma. This sensitivity highlights the necessity for improved models and measurements of the production of secondary craters.

This model implicitly assumes that the secondary SFD maintains a steep slope for all diameters. However, for a steep power-law distribution, the total volume of ejected fragments necessary to produce progressively smaller secondaries eventually exceeds the total mass

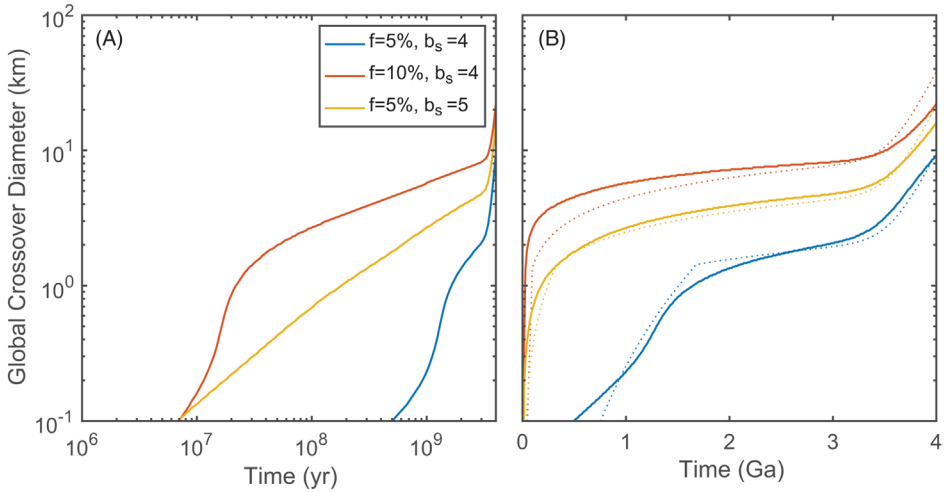

FIGURE 6.7 The global crossover diameter between primary and secondary craters for various values of f and b_s. For (A), time is in log-scale and shows the period from 1 Ma to 4 Ga; For (B), time is linear and focuses on Ga timescales. The primary SFD is determined by the Ivanov PF and the secondary SFD is calculated using Eq. (6.4). The *dotted lines* show the crossover diameter predicted for a hypothetical two-branch primary production: $b_p = 2$ for craters >1 km and $b_p = 3.7$ for craters <1 km. The global crossover diameter is very sensitive to f and b_s, which determine the number of secondaries produced by each primary.

excavated by the primary (Melosh, 1989; McEwen et al., 2005). Therefore steep SFDs cannot continue to arbitrarily small sizes and must level off after some number of secondaries are produced. The number of secondaries that a primary is able to produce is difficult to observe, but perhaps the best estimate comes from young craters with well-preserved secondary fields. Zunil (10.1 km) is estimated to have produced $\sim 10^8$ decameter-sized craters (McEwen et al., 2005; Preblich et al., 2007). Williams (2018) estimate that Corinto crater (13.8 km) produced over 10^9 meter-to-decameter sized secondary craters with fairly steep-sloped SFDs at these sizes. This may continue to smaller sizes, though resolution limitations prevent the observation of this. Additionally, modeling work by McEwen et al. (2005) suggests that the production of this many secondaries does not violate reasonable physical constraints. For surfaces older than a few Ma, global crossover occurs before 10^8 craters are produced (Fig. 6.6). Therefore the results presented in Fig. 6.7 would not be significantly affected for surfaces older than this if 10^8 craters is the appropriate constraint. As the crossover diameter increases with time, the number of secondaries required to reach crossover decreases. For example, the global crossover diameter after 1 Ga occurs at just a few thousand secondary craters (Fig. 6.6).

It is important to note that Fig. 6.7 presents the globally averaged crossover diameter. If these secondaries were uniformly distributed across the surface of Mars, this would imply that 1 km craters could not be used reliably for chronology on Ga old surfaces. However, most secondaries are clustered within the regions proximal to the largest few primaries. These can be easily removed from counts or avoided. The relative abundance of distant field secondaries in regions that are not clearly influenced by nearby large primaries is the more relevant question for crater chronology, and the spatial distribution of secondaries becomes important.

7 Model of the spatial distribution of secondaries

We develop a model which accounts for the spatial distribution of secondary craters. Primary craters are stochastically placed on a Mars-sized surface and each primary produces a distribution of secondaries determined by parameters f and b_s. However, instead of placing secondaries uniformly on the surface, secondary spatial density drops off radially from each primary as $n \propto r^{-\alpha}$ with the maximum spatial density at 2.5 crater radii. Based on our observations of Lomonosov crater, we model secondary accumulation using $f = 10\%$, $b_s = 4$, and α values of 4 and 5 (Fig. 6.5). We also include model results based on Lyot crater ($f = 7\%$, $b_s = 4$, and $\alpha = 3$), which has fewer secondaries than Lomonosov relative to its size but with a more gradual drop-off with distance. However, we note that the parameters determined for Lyot may be influenced by the erasure of secondaries or by regional variations in the background spatial density of primaries (discussed in Section 5.1). For a given simulation, we model the production of all primary and secondary craters that are larger than a specified minimum diameter, which is selected such that $\sim 10^7$ craters are produced in total (e.g., this threshold is 500 m for a 1 Ga surface). The surface is then gridded and the spatial density of primaries and secondaries within each bin is calculated. The local crossover diameter within each bin is determined by extrapolating the SFD of primaries and secondaries to smaller sizes and calculating the diameter at which their differential SFDs intersect. While we apply this model to Mars, it can be adapted for any planetary body if the number and spatial distribution of secondaries produced by primaries is constrained (accounting for differences in gravity, impact velocity, etc.).

Fig. 6.8 shows model results for a 1 Ga surface using parameters: $b_s = 4$, $f = 0.1$, and $\alpha = 5$. Globally, there is an order of magnitude more km-scale secondaries than primaries. Primary craters >1 km are uniformly distributed across the surface with a mean spatial density of $\sim 3 \times 10^{-4}$ km^{-2}. The secondary spatial density can exceed this by several orders of magnitude in regions close to large primaries but is much lower elsewhere. Fig. 6.9A and B show cumulative histograms for primary and secondary crater spatial density compared to the global average. As expected, primary spatial density is normally distributed around the global mean. However, the global mean secondary spatial density is not a good predictor for a typical region on the surface of Mars. For a model run using Lomonosov-like parameters and $\alpha = 5$, the fraction of secondaries larger than 1 km on a median surface (corresponding to a CDF value of 0.5) is ~19%, significantly lower than the global average of ~90%. For a model run using $\alpha = 4$, secondaries are distributed at greater range and ~38% of craters >1 km on a median surface are secondaries. When using Lyot-like parameters, secondaries are even more spatially uniform, but the global mean fraction of secondaries is lower due to fewer secondaries overall. These results agree qualitatively with the modeling results of Bierhaus et al. (2018) for the Moon, who showed that the maximum and minimum spatial densities of secondaries vary quite significantly across the surface compared to the more homogeneous primary population.

Fig. 6.9C presents cumulative histograms showing the spatial variation in crossover diameter for modeled surfaces of various ages. The crossover diameter for a median surface after 1 Ga is between 70 and 300 m depending on the model parameters considered. Fig. 6.10 shows the evolution of the median crossover diameter with time. The median crossover diameter exceeds 1 km on surfaces older than ~1–2 Ga. This suggests that secondaries may contaminate counts for craters of this size on Ga old terrains, even in regions that are not obviously affected by large primaries. However, at 100 Ma the median crossover diameter is less than 10 m, which is about the limit of what can be easily counted

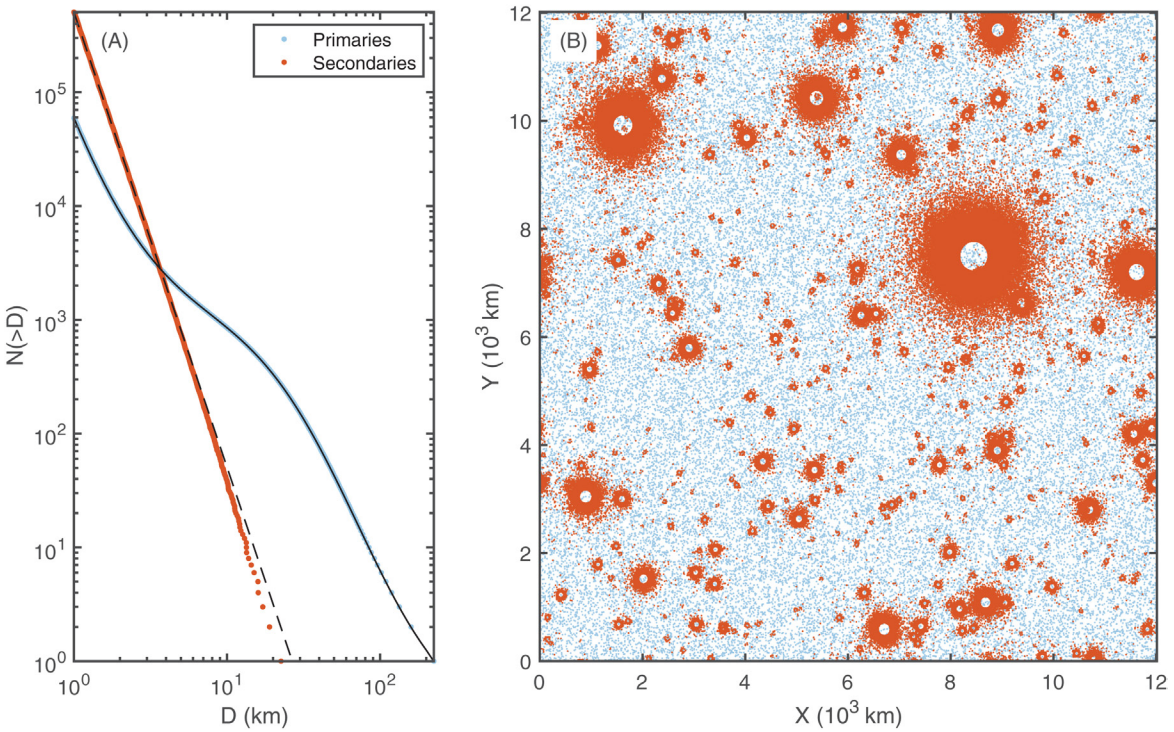

FIGURE 6.8 Example of a simulated (A) size-frequency distribution and (B) map of primary and secondary craters for a Mars-sized surface after 1 Ga. Each primary crater produces secondaries determined by $f = 10\%$, $b_s = 4$, and $\alpha = 5$. For clarity, only craters larger than 1 km are shown. The total number of km-scale secondaries globally is about an order-of-magnitude greater than the number of primaries. However, secondaries are clustered around large primary craters, resulting in some regions with many secondary craters and others with relatively few.

using current orbital imagery. This suggest that distant secondaries should not influence counts on young (<100 Ma) surfaces known to be far from obvious sources of secondary craters. We note that the radial drop-off in secondaries, α, is not well constrained, and further study of the distribution of distant secondaries would help to inform this model. However, any radial drop-off will result in spatial clustering and cause the behavior shown in Figs. 6.8–6.10.

Our model likely overestimates the effect of secondaries in several ways. We do not account for possible focusing of secondaries along rays. Clustering of secondary craters azimuthally would further exaggerate the differences in local secondary spatial density. Additionally, like the analytical model presented in Section 6, the determination of crossover diameter assumes that the secondary SFD maintains a steep slope at all diameters. Steep secondary SFDs cannot extend to arbitrarily small sizes. For reference, the dashed-line segments of Figs. 6.9C and 6.10 show when the calculated crossover diameter requires the largest primary to produce more than 10^8 secondaries. If this is the appropriate threshold for the number of secondaries produced per primary, then our model overestimates local crossover diameters smaller than a few 100 m for Ga surfaces. The solid-line segments would be unaffected by a constraint of 10^8 craters. This model can be improved if the ray structure and number of secondaries per primary are better

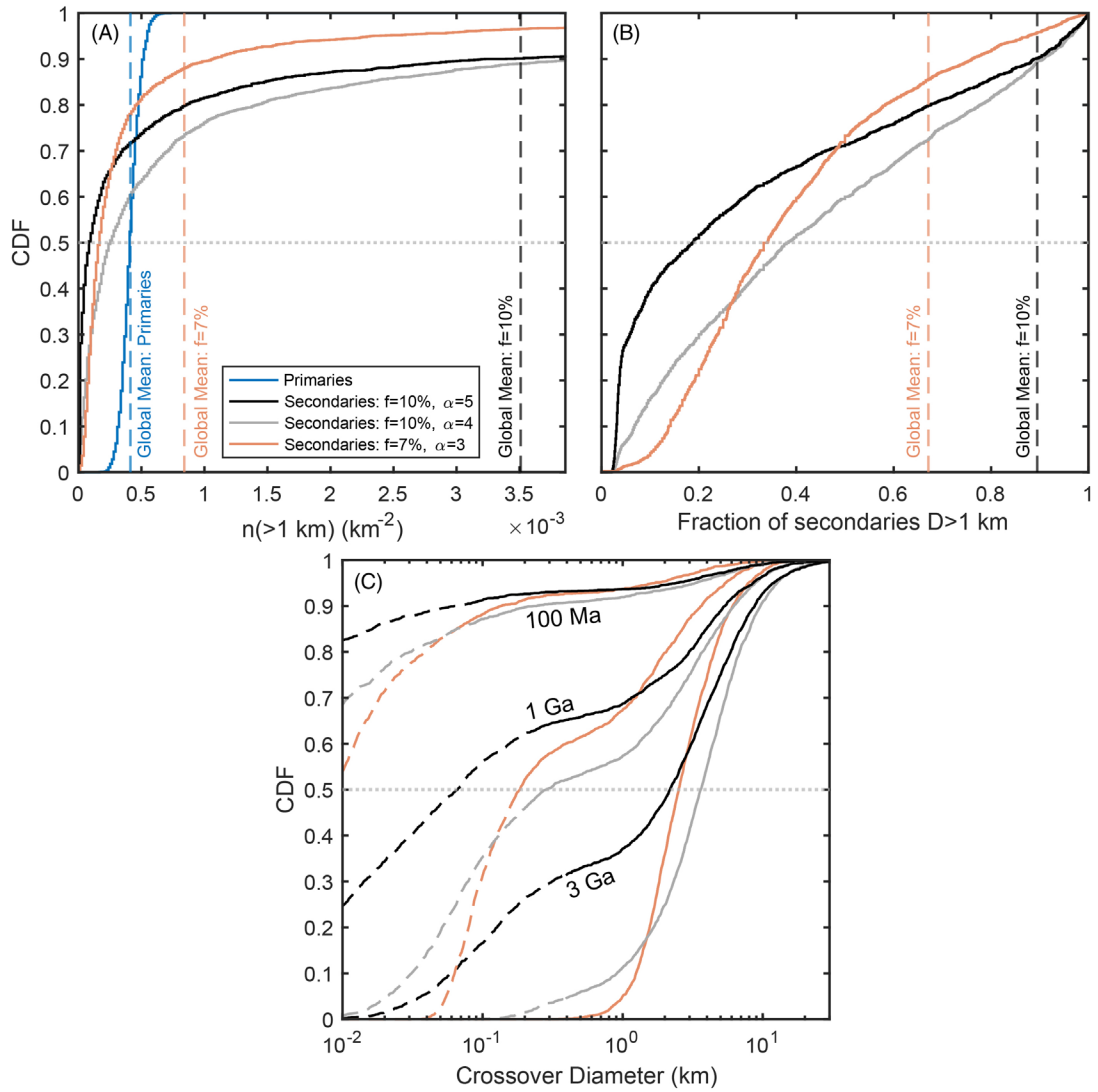

FIGURE 6.9 Primary and secondary accumulation modeled using parameters informed by Lomonosov crater ($f = 10\%$, $b_s = 4$, and α values of 4 and 5) and Lyot crater ($f = 7\%$, $b_s = 4$, and $\alpha = 3$). (A) Cumulative histograms of the spatial density of primary and secondary craters >1 km after 1 Ga. The spatial density of primary craters is normally distributed around the global mean. However, most secondaries are clustered around large primaries and the median secondary spatial density (indicated by a CDF value of 0.5) is significantly lower than the global mean. (B) Cumulative histogram of the local fraction of secondaries >1 km after 1 Ga. (C) Cumulative histograms of the local crossover diameter modeled for 100 Ma, 1 Ga, and 3 Ga. The histograms transition to *dashed lines* when the calculated crossover diameter requires the largest primary to produce more than 10^8 secondaries.

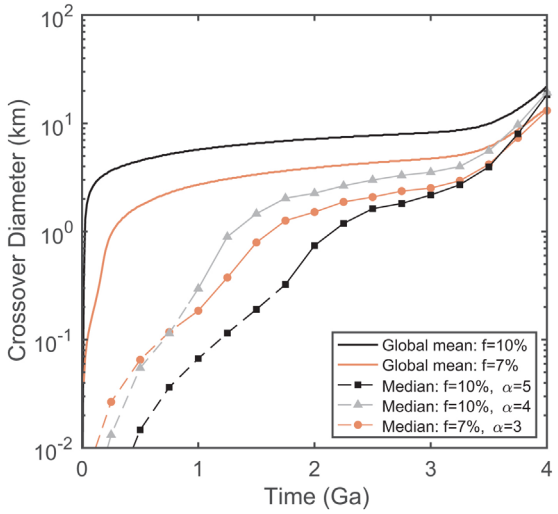

FIGURE 6.10 The global mean and median crossover diameter calculated for Mars using parameters informed by Lomonosov crater ($f = 10\%$, $b_s = 4$ and α values of 4 and 5) and Lyot crater ($f = 7\%$, $b_s = 4$ and $\alpha = 3$). The global mean crossover diameter is calculated using the approach described in Section 6. The median crossover diameter, which accounts for the spatial distribution of secondaries, is significantly less than the global mean and is sensitive to α, which controls the spatial clustering of secondaries around primaries. The *dashed lines* show when the calculated crossover diameter requires the largest primary to produce more than 10^8 secondaries.

understood; however, we prefer to overestimate the contribution of secondaries from these effects in the absence of well-established constraints. This likely overestimate is valuable as it provides crater counters with an upper limit on the largest sizes that may be significantly affected by secondaries.

This model represents a production population and does not account for crater erasure by other craters [i.e., saturation equilibrium (Hartmann, 1984)] or erosion from process like infill [these processes are discussed in Rubanenko et al. (2021) (Chapter 5: Challenges in Crater Chronology on Mars as Reflected in Jezero Crater). In reality, several processes preferentially erase small craters and many of the secondaries produced throughout Mars' past may no longer be observable today. This is apparent in Fig. 6.4, where km-scale craters, both primary and secondary, consistently deviate from the expected PF. Additionally, Lyot crater has the most obvious secondary field for a >200 km crater on Mars (Robbins and Hynek, 2011b), despite there being ~50 craters of similar size or larger on the Martian surface. This indicates that the secondaries of many large primaries have been erased.

8 Conclusions

The observation of impact craters is the principal method for determining surface age throughout the solar system. Large primary craters can generate numerous smaller secondary craters nearly instantaneously. Many of these are distributed close to their primary or within obvious rays and can be excluded from crater counts. However, some distant field secondaries are difficult to differentiate from primaries of the same size. Several young craters on Mars with well-preserved ray systems show that secondaries of a single primary can influence crater counts to distances of ~100 crater radii (McEwen et al., 2005; Quantin et al., 2016; Williams, 2018; Williams et al., 2018). The effect that secondaries have on the validity of crater chronology has been heavily debated and still remains a topic of significant discussion.

We present model results for the global accumulation of secondary craters on Mars, accounting for spatial clustering around large primaries. On Ga timescales the global number of >1 km secondary craters produced may exceed the number of primaries by an order of magnitude. However, most secondaries are contained within a few crater radii of the largest few primary craters. The contribution of distant field secondaries to regions that are far from obvious large primaries is lower. We predict the crossover diameter on a median surface after 1 Ga may be as large as 300 m, significantly lower than the global mean of ~6 km but within the range of crater diameters which may be reasonably used for chronology.

For surfaces younger than ~100 Ma, we predict a median crossover diameter of <10 m, about the limit of what can be easily counted using existing orbital imagery. The median crossover diameter is expected to exceed 1 km on surfaces older than ~1–2 Ga. These results likely overestimate the number of secondaries still visible today, as the secondaries of many old primaries have since been erased. The high spatial variability of secondaries suggests that care should be taken when counting craters on the scale of or smaller than the expected crossover diameter. Because the SFD of secondaries tends to have a steeper slope than that of primaries, an unexpected increase in slope at smaller sizes may indicate the presence of secondary craters.

The global accumulation of secondary craters is sensitive to the number and spatial distribution of secondaries produced by individual primary craters. Several large (~20–220 km) craters on Mars show noticeable enhancements in the number of 1–10 km craters in their nearby regions (Robbins and Hynek, 2011b), likely the result of secondaries. We investigate four of these Martian craters and show that the number of secondaries required to explain the observed excess in km-scale craters is greater than previously thought, assuming no or equal erasure of primaries and secondaries. The spatial density of secondary craters drops off rapidly radially away from these craters, making characterization of secondaries beyond ~8 crater radii difficult. The number and spatial distribution of distant secondaries produced by primaries of various sizes remains poorly constrained. We recommend further study of distant secondary populations to better quantify their SFD, radial distribution, and degree of clustering along rays.

Acknowledgments

The authors would like to thank Michelle Kirchoff and Stuart Robbins for their valuable insight and feedback on the manuscript during the review process. The contributions of J.-P. Williams were funded by a NASA Solar System Workings grant no. 80NSSC18K0010.

References

Arvidson, R., Crozaz, G., Drozd, R.J., Hohenberg, C.M., Morgan, C.J., 1975. Cosmic ray exposure ages of features and events at the Apollo landing sites. Moon 13 (1–3), 259–276.

Baldwin, R.B., 1949. The Face of the Moon. University of Chicago Press, Chicago, IL, 239 pp.

Bierhaus, E.B., Chapman, C.R., Merline, W.J., 2005. Secondary craters on Europa and implications for cratered surfaces. Nature 437 (7062), 1125–1127.

Bierhaus, E.B., Chapman, C.R., Merline, W.J., Brooks, S.M., Asphaug, E., 2001. Pwyll secondaries and other small craters on Europa. Icarus 153 (2), 264–276.

Bierhaus, E.B., McEwen, A.S., Robbins, S.J., Singer, K.N., Dones, L., Kirchoff, M.R., Williams, J.P., 2018. Secondary craters and ejecta across the solar system: populations and effects on impact-crater-based chronologies. Meteorit. Planet. Sci. 53 (4), 638–671.

Bottke, W.F., Vokrouhlický, D., Nesvorný, D., 2007. An asteroid breakup 160 Myr ago as the probable source of the K/T impactor. Nature 449 (7158), 48–53.

Brown, H., 1960. The density and mass distribution of meteoritic bodies in the neighborhood of the earth's orbit. J. Geophys. Res. 65 (6), 1679–1683.

Brown, P., Spalding, R.E., ReVelle, D.O., Tagliaferri, E., Worden, S.P., 2002. The flux of small near-Earth objects colliding with the Earth. Nature 420 (6913), 294–296.

Chapman, C.R., Veverka, J., Belton, M.J., Neukum, G., Morrison, D., 1996. Cratering on Gaspra. Icarus 120 (1), 231–245.

Christensen, P.R., Jakosky, B.M., Kieffer, H.H., Malin, M.C., McSween, H.Y., Nealson, K., Mehall, G.L., Silverman, S.H., Ferry, S., Caplinger, M., Ravine, M., 2004. The Thermal Emission Imaging System (THEMIS) for the Mars 2001 Odyssey Mission. Space Sci. Rev. 110 (1–2), 85–130.

Crater Analysis Techniques Working Group, 1979. Standard techniques for presentation and analysis of crater size-frequency data. Icarus 37 (2), 467–474.

Daubar, I.J., McEwen, A.S., Byrne, S., Kreslavsky, M., Saper, L., & Kennedy, M.R. (2014). New dated impacts on Mars and an updated current cratering rate. 8th International Conference on Mars, Abstract 1007.

Daubar, I.J., McEwen, A.S., Byrne, S., Kreslavsky, M., Saper, L., Kennedy, M.R., Golombek, M.P., 2015. Current state of knowledge of modern Martian cratering. Workshop on Issues in Crater Studies and the Dating of Planetary Surfaces, Abstract 9007.

Daubar, I.J., McEwen, A.S., Byrne, S., Kennedy, M.R., Ivanov, B., 2013. The current Martian cratering rate. Icarus 225 (1), 506–516.

Daubar, I.J., Banks, M.E., Schmerr, N.C., Golombek, M.P., 2019. Recently formed crater clusters on Mars. J. Geophys. Res.: Planets 124 (4), 958–969.

Daubar, I.J., Dundas, C.M., Byrne, S., Geissler, P., Bart, G.D., McEwen, A.S., Russell, P.S., Chojnacki, M., Golombek, M.P., 2016. Changes in blast zone albedo patterns around new Martian impact craters. Icarus 267, 86–105.

Dundas, C.M., McEwen, A.S., 2007. Rays and secondary craters of Tycho. Icarus 186 (1), 31–40.

Edwards, C.S., Nowicki, K.J., Christensen, P.R., Hill, J., Gorelick, N., Murray, K., 2011. Mosaicking of global planetary image datasets: 1. Techniques and data processing for Thermal Emission Imaging System (THEMIS) multispectral data. J. Geophys. Res.: Planets 116 (E10), E10008.

Hartmann, W.K., 1964. On the distribution of lunar crater diameters. Commun. Lunar Planet. Lab. 2, 197–204.

Hartmann, W.K., 1984. Does crater "saturation equilibrium" occur in the solar system? Icarus 60 (1), 56–74.

Hartmann, W.K., 2005. Martian cratering 8: isochron refinement and the chronology of Mars. Icarus 174 (2), 294–320.

Hartmann, W.K., Daubar, I.J., 2017. Martian cratering 11. Utilizing decameter scale crater populations to study Martian history. Meteorit. Planet. Sci. 52 (3), 493–510.

Hartmann, W.K., Daubar, I.J., Popova, O., Joseph, E.C., 2018. Martian cratering 12. Utilizing primary crater clusters to study crater populations and meteoroid properties. Meteorit. Planet. Sci. 53 (4), 672–686.

Hartmann, W.K., Neukum, G., 2001. Cratering chronology and the evolution of Mars. Space Sci. Rev. 96, 165–194.

Holsapple, K.A., 1993. The scaling of impact processes in planetary sciences. Annu. Rev. Earth Planet. Sci. 21 (1), 333–373.

Ivanov, B.A., 2001. Mars/Moon cratering rate ratio estimates. Space Sci. Rev. 96 (1–4), 87–104.

Ivanov, B.A., 2006. Earth/Moon impact rate comparison: searching constraints for lunar secondary/primary cratering proportion. Icarus 183 (2), 504–507.

Ivanov, B.A., Melosh, H.J., & McEwen, A.S. (2014). New small impact craters in high resolution HiRISE images - IV. Lunar and Planetary Science Conference, 45, Abstract 1812.

Kirchoff, M.R., Marchi, S., Bottke, W.F., Chapman, C.R., Enke, B., 2021. Suggestion that recent (≤3 Ga) flux of kilometer and larger impactors in the Earth-Moon system has not been constant. Icarus, 355 114110.

Kreiter, T.J., 1960. Dating lunar surface features by using crater frequencies. Publ. Astron. Soc. Pac. 72 (428), 393–398.

König, B., 1977. Investigations of Primary and Secondary Impact Structures on the Moon and Laboratory Experiments to Study the Ejecta of Secondary Particles. Ph.D. thesis. Ruprecht Karl University of Heidelberg, Baden-Württemberg, Germany, 88 pp.

Malin, M.C., Bell, J.F., Cantor, B.A., Caplinger, M.A., Calvin, W.M., Clancy, R.T., Edgett, K.S., Edwards, L., Haberle, R.M., James, P.B., Lee, S.W., Ravine, M.A., Thomas, P.C., Wolff, M.J., 2007. Context camera investigation on board the Mars Reconnaissance Orbiter. J. Geophys. Res.: Planets 112 (E5), E05S04.

Malin, M.C., Danielson, G.E., Ingersoll, A.P., Masursky, H., Veverka, J., Ravine, M.A., Soulanille, T.A., 1992. Mars observer camera. J. Geophys. Res.: Planets 97 (E5), 7699–7718.

Malin, M.C., Edgett, K.S., Posiolova, L.V., McColley, S.M., Dobrea, E.Z.N., 2006. Present-day impact cratering rate and contemporary gully activity on Mars. Science 314 (5805), 1573–1577.

Mazrouei, S., Ghent, R.R., Bottke, W.F., Parker, A.H., Gernon, T.M., 2019. Earth and Moon impact flux increased at the end of the Paleozoic. Science 363 (6424), 253–257.

McEwen, A.S., Bierhaus, E.B., 2006. The importance of secondary cratering to age constraints on planetary surfaces. Annu. Rev. Earth Planet. Sci. 34, 535–567.

McEwen, A.S., Eliason, E.M., Bergstrom, J.W., Bridges, N.T., Hansen, C.J., Delamere, W.A., Grant, J.A., Gulick, V.C., Herkenhoff, K.E., Keszthelyi, L., Kirk, R.L., Mellon, M.T., Squyres, S.W., Thomas, N., Weitz, C.M., 2007. Mars Reconnaissance Orbiter's High Resolution Imaging Science Experiment (HiRISE). J. Geophys. Res.: Planets 112 (E5), E05S02.

McEwen, A.S., Preblich, B.S., Turtle, E.P., Artemieva, N.A., Golombek, M.P., Hurst, M., Kirk, R.L., Burr, D.M., Christensen, P.R., 2005. The rayed crater Zunil and interpretations of small impact craters on Mars. Icarus 176 (2), 351–381.

Melosh, H.J., 1989. Impact Cratering: A Geologic Process. Oxford University Press, New York, NY, 245 pp..

Nesvorný, D., Vokrouhlický, D., Morbidelli, A., Bottke, W.F., 2009. Asteroidal source of L chondrite meteorites. Icarus 200 (2), 698–701.

Neukum, G., 1983. Meteoritenbombardement und Datierung planetarer Oberflachen. Habilitation Dissertation for faculty membership. Ludwig-Maximillians-University, Munich, Germany. 186 pp.

Neukum, G., Ivanov, B.A., 1994. Crater size distributions and impact probabilities on Earth from lunar, terrestrial-planet, and asteroid cratering data. In: Gehrels, T. (Ed.), Hazards Due to Comets and Asteroids. University of Arizona Press, Tucson, AZ, pp. 359-416.

Neukum, G., Ivanov, B.A., Hartmann, W.K., 2001. Cratering records in the inner solar system in relation to the lunar reference system. Space Sci. Rev. 96, 55–86.

Neukum, G., König, B., Arkani-Hamed, J., 1975. A study of lunar impact crater size-distributions. Moon 12 (2), 201–229.

Öpik, E.J., 1960. The lunar surface as an impact counter. Mon. Not. R. Astron. Soc. 120 (5), 404–411.

Popova, O., Nemtchinov, I., Hartmann, W.K., 2003. Bolides in the present and past Martian atmosphere and effects on cratering processes. Meteorit. Planet. Sci. 38 (6), 905–925.

Preblich, B.S., McEwen, A.S., Studer, D.M., 2007. Mapping rays and secondary craters from the Martian crater Zunil. J. Geophys. Res.: Planets 112 (E5), E05006.

Quantin, C., Popova, O., Hartmann, W.K., Werner, S.C., 2016. Young Martian crater Gratteri and its secondary craters. J. Geophys. Res.: Planets 121 (7), 1118–1140.
Robbins, S.J., 2014. New crater calibrations for the lunar crater-age chronology. Earth Planet. Sci. Lett. 403, 188–198.
Robbins, S.J., Hynek, B.M., 2011a. Distant secondary craters from Lyot crater, Mars, and implications for surface ages of planetary bodies. Geophys. Res. Lett. 38 (5), L05201.
Robbins, S.J., Hynek, B.M., 2011b. Secondary crater fields from 24 large primary craters on Mars: insights into nearby secondary crater production. J. Geophys. Res.: Planets 116 (E10), E10003.
Robbins, S.J., Hynek, B.M., 2012. A new global database of Mars impact craters ≥1 km: 1. Database creation, properties, and parameters. J. Geophys. Res.: Planets 117 (E5), E05004.
Robbins, S.J., Hynek, B.M., 2014. The secondary crater population of Mars. Earth Planet. Sci. Lett. 400, 66–76.
Roberts, W.A., 1964. Secondary craters. Icarus 3 (4), 348–364.
Rubanenko, L., Powell, T.M., Williams, J.-P., Daubar, I., Edgett, K.S., Paige, D.A., 2021. Challenges in crater chronology on Mars as reflected in Jezero crater. In: Soare, R.J., Conway, S.J., Williams, J.-P., Oehler, D.Z. (Eds.), Mars Geological Enigmas: From the Late Noachian Epoch to the Present Day. Elsevier Books, Amsterdam, The Netherlands.
Schmidt, R.M., Holsapple, K.A., 1982. Estimates of crater size for large-body impact: gravity-scaling results. Spec. Pap. Geol. Soc. Am. 190, 93–102.
Schmidt, R.M., Housen, K.R., 1987. Some recent advances in the scaling of impact and explosion cratering. Int. J. Impact Eng. 5 (1–4), 543–560.
Schultz, P.H., Singer, J., 1980. A comparison of secondary craters on the Moon, Mercury, and Mars. Lunar Planet. Sci. Conf. Proc. 11, 2243–2259.
Shoemaker, E.M., 1965. Preliminary analysis of the fine structure of Mare Cognitum. In: Hess, W.N., Menzel, D.H., O'Keefe, J.A. (Eds.), The Nature of the Lunar Surface. Johns Hopkins Press, Baltimore, MD, pp. 23–77.
Shoemaker, E.M., Hackman, R.J., Eggleton, R.E., 1963. Interplanetary correlation of geologic time. Adv. Astronaut. Sci. 8, 70–89.
Singer, K.N., Jolliff, B.L., McKinnon, W.B., 2020. Lunar secondary craters and estimated ejecta block sizes reveal a scale-dependent fragmentation trend. J. Geophys. Res.: Planets 125 (8), e2019JE006313.
Smith, D.E., Zuber, M.T., Frey, H.V., Garvin, J.B., Head, J.W., Muhleman, D.O., Pettengill, G.H., Phillips, R.J., Solomon, S.C., Zwally, H.J., Banerdt, W.B., Duxbury, T.C., Golombek, M.P., Lemoine, F.G., Neumann, G.A., Rowlands, D.D., Aharonson, O., Ford, P.G., Ivanov, A.B., Johnson, C.L., McGovern, P.J., Abshire, J.B., Afzal, R.S., Sun, X., 2001. Mars Orbiter Laser Altimeter: experiment summary after the first year of global mapping of Mars. J. Geophys. Res.: Planets 106 (E10), 23689–23722.
Soderblom, L.A., Condit, C.D., West, R.A., Herman, B.M., Kreidler, T.J., 1974. Martian planetwide crater distributions: implications for geologic history and surface processes. Icarus 22 (3), 239–263.
Speyerer, E.J., Povilaitis, R.Z., Robinson, M.S., Thomas, P.C., Wagner, R.V., 2016. Quantifying crater production and regolith overturn on the Moon with temporal imaging. Nature 538 (7624), 215–218.
Stöffler, D., Ryder, G., 2001. Stratigraphy and isotope ages of lunar geologic units: chrono-logical standard for the inner solar system. Space Sci. Rev. 96, 9–54.
Terada, K., Morota, T., Kato, M., 2020. Asteroid shower on the Earth-Moon system immediately before the Cryogenian period revealed by KAGUYA. Nat. Commun. 11 (1), 1–10, https://doi.org/10.1038/s41467-020-17115-6.
Tornabene, L.L., Moersch, J.E., McSween, Jr., H.Y., McEwen, A.S., Piatek, J.L., Milam, K.A., Christensen, P.R., 2006. Identification of large (2–10 km) rayed craters on Mars in THEMIS thermal infrared images: implications for possible Martian meteorite source regions. J. Geophys. Res.: Planets 111 (E10), E10006.
Vickery, A.M., 1986. Size-velocity distribution of large ejecta fragments. Icarus 67 (2), 224–236.
Vickery, A.M., 1987. Variation in ejecta size with ejection velocity. Geophys. Res. Lett. 14 (7), 726–729.
Vokrouhlický, D., Bottke, W.F., Nesvorný, D., 2017. Forming the Flora family: implications for the near-Earth asteroid population and large terrestrial planet impactors. Astron. J. 153 (4), 172.
Werner, S.C., Ivanov, B.A., Neukum, G., 2009. Theoretical analysis of secondary cratering on Mars and an image-based study on the Cerberus Plains. Icarus 200 (2), 406–417.
Wilhelms, D.E., Oberbeck, V.R., Aggarwal, H.R., 1978. Size-frequency distributions of primary and secondary lunar impact craters. Lunar Planet. Sci. Conf. Proc. 9, 3735–3762.
Williams, J.-P., 2018. Modification of the Martian surface by impact cratering. In: Soare, R., Conway, S., Clifford, S. (Eds.), Dynamic Mars: Recent and Current Landscale Evolution of the Red Planet. Elsevier Books, Amsterdam, The Netherlands, pp. 365–386, https://doi.org/10.1016/B978-0-12-813018-6.00012-1.
Williams, J.P., Pathare, A.V., Aharonson, O., 2014. The production of small primary craters on Mars and the Moon. Icarus 235, 23–36.
Williams, J.P., van der Bogert, C.H., Pathare, A.V., Michael, G.G., Kirchoff, M.R., Hiesinger, H., 2018. Dating very young planetary surfaces from crater statistics: a review of issues and challenges. Meteorit. Planet. Sci. 53 (4), 554–582.
Young, J., 1940. A statistical investigation of diameter and distribution of lunar craters. J. Br. Astron. Assoc. 50 (9), 309–326.